Femtosecond coherent control of thermal photoassociation of magnesium atoms

Leonid Rybak,[a] Zohar Amitay,*[a] Saieswari Amaran,[b] Ronnie Kosloff,*[b] Michał Tomza,[c] Robert Moszynski[c] and Christiane P. Koch[d]

Received 1st April 2011, Accepted 12th May 2011
DOI: 10.1039/c1fd00052g

We investigate femtosecond photoassociation of thermally hot atoms in the gas phase and its coherent control. In the photoassociation process, formation of a chemical bond is facilitated by light in a free-to-bound optical transition. Here, we study free-to-bound photoassociation of a diatomic molecule induced by femtosecond pulses exciting a pair of scattering atoms interacting *via* the van-der-Waals-type electronic ground state potential into bound levels of an electronically excited state. The thermal gas of reactants is at temperatures in the range of hundreds of degrees. Despite this incoherent initial state, rotational and vibrational coherences are observed in the probing of the created Mg_2 molecules.

1 Introduction

Coherent control was initiated as a scheme to steer a chemical reaction to its desired outcome.[1] In a nutshell, the quantum interference is employed to constructively enhance the selected product and destructively suppress the other possible channels.[2] A prerequisite for such control is coherent dynamics from the initial state to the final product.[3,4] The control is obtained by an external field which can alter the dynamics, typically by temporarily altering the generator—the Hamiltonian. For the standard situation describing single-photon transition, it reads

$$\hat{\mathbf{H}} = \hat{\mathbf{H}}_0 - \hat{\mu}\cdot\varepsilon(t)\,, \tag{1}$$

where $\hat{\mathbf{H}}_0$ is the bare molecular Hamiltonian, $\hat{\mu}$ the electric dipole moment operator, and $\varepsilon(t)$ the time-dependent external electric field. In a two-photon setting employing adiabatic elimination of all the off-resonant single-photon transitions, a Hamiltonian with a structure similar to that of eqn (1) is obtained except for the molecule-light coupling where the external field enters quadratically.[5]

Coherent control of chemical reactions has been achieved experimentally.[6,7] Almost exclusively, all demonstrations were unimolecular reactions such as photodissociation or photoisomerization. Coherent control of binary reactions with photoassociation as one prominent example has proven to be a much harder task.[8,9] The difficulty originates from the initial state of the reaction. In a unimolecular reaction the final fragments are initially entangled. As a result a coherent pathway connects

[a]*The Shirlee Jacobs Femtosecond Laser Research Laboratory, Schulich Faculty of Chemistry, Technion - Israel Institute of Technology, Haifa, 32000, Israel. E-mail: amitayz@tx.technion.ac.il*
[b]*Institute of Chemistry and The Fritz Haber Research Center, The Hebrew University, Jerusalem, 91904, Israel. E-mail: ronnie@fh.huji.ac.il*
[c]*Department of Chemistry, University of Warsaw, Pasteura 1, 02-093 Warsaw, Poland*
[d]*Theoretische Physik, Universität Kassel, Heinrich-Plett-Str. 40, 34132 Kassel, Germany*

the initial state to the final outcome. To control binary chemical reactions a prerequisite is to entangle the initial state.[10] In ultracold conditions, initial entanglement is present due to threshold effects such that only a few partial waves of the colliding pair can lead to association.[11,12] In thermal conditions, many partial waves participate and the colliding pair becomes unentangled.

Is coherent control of a binary reaction in a thermal state possible? The answer depends on the ability to filter out an entangled sub-ensemble of binary states. In the present study we demonstrate that a binary sub-ensemble with high purity is filtered out from a thermal ensemble of hot atoms. Moreover molecular coherence is generated. This is the prerequisite for coherent control of binary reactions.

The experiment is based on two-photon photoassociation of hot magnesium atoms to form a bound molecule. Magnesium in its electronic ground state is a closed shell atom. Therefore only a weak van der Waals attractive well can be found in the ground electronic potential of Mg_2 ($X^1\Sigma_g^+$). Upon promoting an electron to the π orbital, a strong chemical bound is formed in the $(1)^1\Pi_g$ state with a binding energy of $\sim$1.8 eV or, equivalently, $\sim$14500 cm^{-1}. This transition is induced by a femtosecond pulse of 70 fs transform-limited duration with a central wavelength of 840 nm. The energy difference corresponds to a two-photon transition. Two photon transition selection rules differ from the common one-photon photoassociation. As a result hidden potentials become accessible. Photoassociation of ultracold atoms takes place at comparatively long inter-atomic distances[13] where the two-photon transition matrix elements between the electronic ground state and the $(1)^1\Pi_g$ excited state vanish. Different from the ultracold regime, photoassociation of hot atoms occurs close to the repulsive wall of the ground state potential due to thermal population of high partial waves. The initial conditions for the experiment are a hot vapor of Mg atoms ($T \sim 1000$ K) in Ar buffer gas. The hot conditions imply a broad distribution of linear and angular momentum of the randomly colliding Mg atoms. A major task of the excitation pulse is to preselect a sub-ensemble with increased purity and coherence.

A time-delayed femtosecond probe pulse interrogates the excited dimer *via* a one-photon excitation to a higher excited electronic state ($(1)^1\Pi_u$). This state has a strong one-photon transition back to the ground state. The corresponding experimental observable is the intensity of the resulting UV fluorescence ($\sim$290 nm) measured as a function of the pump–probe time delay. An oscillating time-dependent signal is a manifestation of coherent dynamics in the $(1)^1\Pi_g$ state. The present experiment is the first two-photon photoassociation experiment where the creation of molecular coherence out of an incoherent atomic ensemble is demonstrated. It is also the first hot femtosecond photoassociation experiment where the observed coherence is of both vibrational and rotational nature.

2 Experimental setup and theoretical model

The sequence of events that constitute the experiment is described in Fig. 1. A two-photon broadband transition promotes a pair of Mg atoms to an electronically excited state ($(1)^1\Pi_g$), forming Mg_2 molecules. After a time delay, a probe photon is absorbed transferring the molecules to a higher excited state ($(1)^1\Pi_u$). Emission from the $(1)^1\Pi_u$ state back to the ground state is detected. This signal as a function of the time delay between pump and probe pulse, yielding a pump–probe signal trace, is the main observable in the present study.

2.1 The experiment

The experiments are conducted in a static cell with Ar buffer gas heated to 1000 K, at which the pressure of the Mg vapor is around 5 Torr. The 840 nm 70 fs linearly-polarized pump and probe femtosecond pulses irradiate the sample at 1 kHz repetition rate in a collinear configuration. The measured signal results from the UV

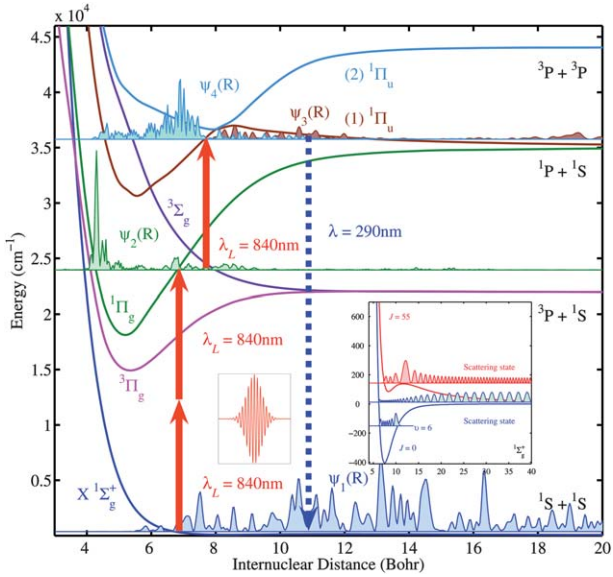

Fig. 1 Two-photon photoassociation of magnesium atoms followed by absorption of a third photon: The relevant potential energy curves are shown with the two-photon and single-photon transitions indicated by red arrows. The experimentally observed fluorescence at ~290 nm is attributed to the dipole-allowed $(1)^1\Pi_u \rightarrow X^1\Sigma_g^+$ transition (blue arrow). A single realization of the random-phase thermal wavefunction used as initial state is displayed on the ground state potential. The wavefunctions on the electronically excited states correspond to times $t = 320$ fs on the $^1\Pi_g$ potential and $t = 640$ fs on the $^1\Pi_u$ potentials. The inset shows a zoom of the ground state potential with vibrational eigenfunction $v = 6$, $J = 0$ and some representative scattering wavefunctions for $J = 0$ and $J = 55$. Note that for high partial waves such as $J = 55$, the potential $V_g(R) + \dfrac{J(J+1)\hbar^2}{2\mu R^2}$ does not contain any bound levels.

fluorescence at ~290 nm that is emitted (with a lifetime of a few ns) toward the direction of the beam entrance and collected there at a small angle from the beam axis using a proper optical setup. The final pump–probe trace results from an average over several scans, which averages out most of the interferometric signature existing in a single trace due to the collinear beam configuration.

2.2 Initial state

The thermal initial state is composed of Mg atoms at a temperature of 1000 K. Magnesium atoms in the ground state have a closed electronic shell. As a result, the $X^1\Sigma_g^+$ ground state potential has no chemical bond. The attraction on this surface is due to a shallow van der Walls well of a depth of approximately 400 cm^{-1}. At the high temperature of the experiment, scattering states up to ~1000 cm^{-1} above threshold are thermally populated. For a Franck–Condon window at an interatomic distance of ~7 bohr, corresponding to a two-photon excitation at 840 nm, angular momentum of up to $J = 100$ can contribute to the process. The centrifugal barrier at this angular momentum eliminates completely the small potential well of the ground surface (*cf.* inset in Fig. 1). For high values of angular momentum, existence of molecules before photoassociation can therefore be excluded. This is another difference compared to photoassociation of ultracold atoms where a few molecules are already produced by the trapping lasers.[14,15] Some exemplary bound states and scattering states of the ground potential surface are shown in the inset of Fig. 1.

Theoretically the initial state is modeled by a thermal density operator composed of bound and scattering states.[11] We eliminate the center of mass motion and consider the density operator of the relative motion of a pair of atoms,

$$\hat{\rho}_T(t=0) = \frac{1}{Z} e^{-\frac{\hat{\mathbf{H}}_g}{k_B T}}, \tag{2}$$

where Z denotes the partition function, $Z = \mathbf{Tr}\left\{ e^{-\frac{\hat{\mathbf{H}}_g}{k_B T}} \right\}$, and $\hat{\mathbf{H}}_g = \frac{\hat{\mathbf{P}}^2}{2\mu} + \hat{\mathbf{V}}_g$ is the Hamiltonian for nuclear motion in the electronic ground state. k_B is the Boltzmann constant and T is the temperature. We decompose this state into partial waves leading to

$$\hat{\rho}_T(t=0) = \sum_J (2J+1)\hat{\rho}_{T,J}, \tag{3}$$

where $\hat{\rho}_{T,J} = \frac{1}{z_J} e^{-\frac{\hat{\mathbf{H}}_J}{k_B T}}$ and $\hat{\mathbf{H}}_J = -\frac{\hbar^2}{2\mu}\frac{\partial^2}{\partial R^2} + V_g(R) + \frac{J(J+1)\hbar^2}{2\mu R^2}$ with $V_g(R)$ is the rotationless electronic ground state potential. z_J is the partition function for a given J. Each initial angular momentum component is modeled separately and the final results are summed. We employ an initial random phase thermal wavefunction to model the dynamics. More details on the method of calculation are reported elsewhere.[16]

2.3 Potential energy curves and transition matrix elements

The first step in simulating the dynamics is to generate the potential energy surfaces described in Fig. 1. In addition, two-photon transition matrix elements and dynamical Stark shifts are required. State-of-the-art *ab initio* techniques have been applied to compute the potential energy curves of the magnesium dimer in the Born–Oppenheimer approximation. In all calculations the aug-cc-pVQZ basis set of quadruple zeta quality as the atomic basis for Mg was used. This basis set was augmented by the set of bond functions consisting of [3*s*3*p*2*d*2*f*1*g*1*h*] functions placed in the middle of Mg_2 dimer bond.

The ground $X^1\Sigma_g^+$ state potential was computed with the coupled cluster method restricted to single, double, and noniterative triple excitations, CCSD(T). For the excited $(1)^1\Pi_g$ and $(1)^1\Pi_u$ states we used the linear response theory (equation of motion approach) within the coupled-cluster singles and doubles framework, LRCCSD. The potential energy curve of the excited $(2)^1\Pi_u$ state in the region of the minimum of the potential was also obtained with the LRCCSD method, whereas at larger internuclear distances this potential energy curve was represented by the multipole expansion with electrostatic and dispersion terms C_n/R^n up to and including $n = 10$. The calculated potentials are shown in Fig. 1. More details on the *ab initio* calculations and spectroscopic characteristics of various electronic states of Mg_2 will be reported elsewhere.[17]

The electric transition dipole moments between states i and f, $\mu_j = \langle \Psi_i | \hat{\mu}_j | \Psi_f \rangle$, where the electric dipole operator, $\hat{\mu}_j = r_j$ is given by the jth component of the position vector and $\Psi_{i/f}$ are the wave functions for the initial and final states. These terms were computed as the first residue of the LRCCSD linear response function for $X^1\Sigma_g^+$, $(1)^1\Pi_g$, and $(1)^1\Pi_u$ states, whereas for transitions to $(2)^1\Pi_u$ state MRCI method was applied. Nonadiabatic radial and angular coupling matrix elements, as well as the spin–orbit coupling matrix elements have been evaluated with the MRCI method. The adiabatic $(1)^1\Pi_u$ and $(2)^1\Pi_u$ states are strongly coupled by the nuclear momentum operator $\hat{\mathbf{P}}_R = i\nabla_R/\mu$, where μ is the reduced mass of Mg_2. We include this non-adiabatic coupling in the model by switching to the diabatic representation.

We adiabatically eliminate intermediate states that are accessed by single-photon transitions and calculate an effective two-photon coupling,

$$\chi(R) = \frac{1}{4}|S(t)|^2 \sum_{i,j} E_i E_j M_{ij}^{f\leftarrow 0}(\omega_L, R) \ , \tag{4}$$

with $S(t)$ being the envelope of the electric field of the laser pulse and E_i being its maximal amplitude, and with ω_L being the pulse carrier frequency in energy units. It is given in terms of the tensor elements of the two-photon transition moment between the ground 0 and excited f state,

$$M_{ij}^{f\leftarrow 0}(\omega_L, R) = -\sum_{n\neq 0}\left[\frac{\langle f|\hat{\mu}_i|n\rangle\langle n|\hat{\mu}_j|0\rangle}{\omega_{n0}-\omega_L} + \frac{\langle f|\hat{\mu}_j|n\rangle\langle n|\hat{\mu}_i|0\rangle}{\omega_{nf}+\omega_L}\right], \tag{5}$$

where $\omega_{nk} = \omega_n - \omega_k$ is the energy difference between states n and k.

In practice, it can be obtained as a residue of the cubic response function.[18] For transitions between the $X^1\Sigma_g^+$ and $(1)^1\Pi_g$ states, $M_{ij}^{f\leftarrow 0}(\omega_L, R)$ was computed as a residue of the coupled cluster cubic response function with electric dipole operators and wave functions within the CCSD framework.[19,20]

Strong field conditions require to include dynamical Stark shifts. The Stark shift of electronic state k can be expressed through the elements of the dynamic electric dipole polarizability tensor,

$$\omega_k^S(t, R) = -\frac{1}{4}|S(t)|^2 \sum_{i,j} E_i E_j \alpha_{ij}^k(\omega_L, R), \tag{6}$$

where the tensor elements of the dynamic polarizability are given by

$$\alpha_{ij}^k(\omega_L, R) = \sum_{n\neq k}\left[\frac{\langle k|\hat{\mu}_i|n\rangle\langle n|\hat{\mu}_j|k\rangle}{\omega_{nk}-\omega_L} + \frac{\langle k|\hat{\mu}_j|n\rangle\langle n|\hat{\mu}_i|k\rangle}{\omega_{nk}+\omega_L}\right]. \tag{7}$$

The tensor elements of the polarizability of the ground $^1\Sigma_g^+$ state were obtained as a coupled cluster linear response function with electric dipole operators and wave functions within CCSD framework.[21]

Dynamic polarizabilities of the exited states were computed as double residues of the coupled cluster cubic response function with electric dipole operators and wave functions within CCSD framework.[22,23]

2.4 Two-photon excitation

The photoassociation step is carried out by a two-photon transition from the $X^1\Sigma_g^+$ electronic ground state to the $(1)^1\Pi_g$ excited state. The photoassociation is induced by a femtosecond pulse of 70 fs transform-limited duration, 840 nm central wavelength, and a transform-limited peak intensity of approximately 5×10^{12} W cm^{-2}.

The transition takes place in a small Franck–Condon window at $R_L \sim 7$ bohr. This two-photon excitation is impulsive on the timescale of vibrational and rotational periods on the excited $(1)^1\Pi_g$ surface (~175 fs and ~0.5–1 ps, respectively). As a result, coherent transient dynamics is generated on this potential. Indirect experimental evidence for populating the $(1)^1\Pi_g$ state comes from emission lines terminating on the excited triplet ^3P atomic Mg state. The origin of these triplet atoms is most probably a nonadiabatic spin–orbit induced transfer from the singlet $(1)^1\Pi_g$ state to the triplet $(1)^3\Pi_g$ close to the inner turning point and to the $(1)^3\Sigma_g$. We calculated the lifetime on the surface to be ~11 ps. The population on this state will dissociate into ^3P atoms (*cf.* Fig. 1).

The excitation dynamics was simulated by solving the time-dependent Schrödinger equation,

$$i\hbar\frac{\partial\Psi}{\partial t} = \hat{\mathbf{H}}_{pump}(t)\Psi\ , \tag{8}$$

where Ψ is a multi-surface wavefunction. The dynamics are generated by the time-dependent Hamiltonian,

$$\hat{\mathbf{H}}_{pump}(t) = \begin{pmatrix} \hat{\mathbf{H}}_g & \chi(t)e^{i\phi(t)} & 0 & 0 \\ \chi(t)e^{-i\phi(t)} & \hat{\mathbf{H}}_e & V_{SO1} & V_{SO2} \\ 0 & V_{SO1} & \hat{\mathbf{H}}_{im1} & V_{SO3} \\ 0 & V_{SO2} & V_{SO3} & \hat{\mathbf{H}}_{im2} \end{pmatrix}, \tag{9}$$

where $\hat{\mathbf{H}}_i$ is the nuclear Hamiltonian, given by $\hat{\mathbf{H}}_{g(e)} = \hat{\mathbf{T}}_{g(e)} + V_{g(e)}(R) + \omega^{S}_{g(e)}(t,R)$. $\hat{\mathbf{T}}_{g(e)}$ is the vibrational and rotational kinetic energy, $V_{g(e)}(R)$ the potential energy, and $\omega^{S}_{g(e)}(t,R)$ the dynamic Stark shift. Here, g corresponds to the $X^1\Sigma_g^+$ state and e to the $^1\Pi_g$ state. $im1$ and $im2$ are the two intermediate triplet states, $(1)^3\Sigma_g$ and $(1)^3\Pi_g$, respectively. The Hamiltonian of the intermediate states is given by $\hat{\mathbf{H}}_{im1(im2)} = \hat{\mathbf{T}}_{im1(im2)} + V_{im1(im2)}(R)$. $V_{SO1(SO2,\ SO3)}$ are the spin–orbit couplings. The transition is driven by the effective two-photon coupling $\chi(R)$, *cf.* eqn (4), and $\phi(t)$ is the time-dependent two-photon phase which is zero for transform-limited pulses.

The Hamiltonian is represented on a grid of length $R_{\min} = 3.0$ bohr to $R_{\max} = 40.0$ bohr, with 1024 grid points. The photoassociation is studied numerically by solving the time-dependent Schrödinger equation for the effective Hamiltonian in eqn (9) with a Chebychev propagator.[24,25] We simulate the dynamics with a pulse duration of 100 fs full-width at half-maximum of (FWHM, with respect to the field) for the transform-limited pulse and a central wavelength of 840 nm. Intensity values were calculated in the range of 10^{10} W cm^{-2} to 10^{13} W cm^{-2}, *cf.* Fig. 2. This pulse corresponds to the experimental 70 fs pulse (where the FWHM is taken with respect to the intensity profile).

We can estimate the purity of the sub-ensemble in the electronically excited state by constructing the corresponding density operator,

$$\hat{\rho}_e(t) = \hat{\mathbf{P}}_e\hat{\rho}_T(t)\hat{\mathbf{P}}_e, \tag{10}$$

where $\hat{\mathbf{P}}_e$ is the projector onto the $(1)^1\Pi_g$ excited state. The normalized excited state purity becomes

$$\mathscr{P}_e = \frac{\mathbf{Tr}[\hat{\rho}_e^2]}{\mathbf{Tr}[\hat{\mathbf{P}}_e\hat{\rho}_T(t)]}\ . \tag{11}$$

The coherence measure C_e in the excited state allows one to characterize the dynamical contribution to the purity.[26] It is obtained by substracting from $\hat{\rho}_e$ the diagonal elements in the energy representation, squaring and taking the trace. Details of the computational details will be described elsewhere.[16]

2.5 The probe step

The main experimental observable is an emission signal at ~290 nm that is emitted following the (2⊕1) absorption of 840 nm photons, *i.e.*, two-photon absorption followed by a time-delayed one-photon absorption. This emission is measured as a function of the time delay between the two-photon and single-photon transitions. The transient signal is associated with the dynamics in the $(1)^1\Pi_g$ excited state. The Fourier transform of this signal should unravel the vibrational and rotational periods on this potential.

We simulate the experimental signal assuming that the population on the $^1\Pi_u$ states is proportional to the emission signal. The pulse parameters remain the same as those of the two-photon pulse. The simulation involves a total of five potential energy surfaces. The initial state for the probe step is $(1)^1\Pi_g$ (denoted as 'g'), the

target states, $(1)^1\Pi_u$ and $(2)^1\Pi_u$, are denoted by '*e*1' and '*e*2', respectively. The intermediate states $(1)^3\Sigma_g^+$ (denoted as *im*1) and $(1)^3\Pi_g$ (denoted as *im*2) are coupled to the 'initial' state $(1)^1\Pi_g$ state by spin–orbit coupling. As discussed in Sec. 2.3, the two $^1\Pi_u$ states exhibit a strong non-adiabatic coupling around the region $R = 8.1$ bohr. Hence, an adiabatic-to-diabatic transformation is performed over these two states and the corresponding diabatic potentials and the diabatic couplings are employed in the simulations.

The Hamiltonian for the probe-pulse simulations is given by

$$\hat{\mathbf{H}}_{probe}(t) = \begin{pmatrix} \hat{\mathbf{H}}_g & \mu_d^1(R)\varepsilon(t) & \mu_d^2(R)\varepsilon(t) & V_{SO1} & V_{SO2} \\ \mu_d^1(R)\varepsilon^*(t) & \hat{\mathbf{H}}_{e1} & V_{12}^d & 0 & 0 \\ \mu_d^2(R)\varepsilon^*(t) & V_{12}^d & \hat{\mathbf{H}}_{e2} & 0 & 0 \\ V_{SO1} & 0 & 0 & \hat{\mathbf{H}}_{im1} & V_{SO3} \\ V_{SO2} & 0 & 0 & V_{SO3} & \hat{\mathbf{H}}_{im1} \end{pmatrix}, \quad (12)$$

where $\mu_d^{1,2}$ are the transition dipole operators in the diabatic basis between the $^1\Pi_u$ states and the $(1)^1\Pi_g$ state, and $\varepsilon(t)$ is the electric field of the laser pulse. $V_{12}{}^d$ denotes the diabatic coupling between the $(1)^1\Pi_u$ and $(2)^1\Pi_u$ states. The simulation includes only vibrational dynamics, *i.e.*, J is kept fixed.

3 Evidence of coherence

The experimental pump–probe trace for the observed fluorescence and its Fourier transform spectra are shown in Fig. 4 for two pulse bandwidth cases: 70 fs and 100 fs transform-limited pulse duration. Even though the theoretical calculations have been conducted with 70 fs pulse, the 100 fs case is shown here for completion. Both pump–probe traces exhibits time dependence long after the pump (photo-associating) pulse is over, hence they reveal molecular rovibrational coherence of the photoassociated Mg_2 molecules. The Fourier spectra of the pump–probe traces show broad peaks at 5.8 THz and 1.2 THz. The former fits a probed vibrational dynamics in the $(1)^1\Pi_g$ state with vibrational levels around $v \sim 30$–50, while the latter fits a probed rotational dynamics in the $(1)^1\Pi_g$ state with rotations around $J \sim 40$–100. As seen, the vibrational coherence is attenuated for the 100 fs pulse as compared to the 70 fs pulse.

In the theoretical description, it is the autocorrelation function, *cf.* Fig. 3, that reflects the dynamics in the $(1)^1\Pi_g$ excited state after the pump pulse. We compare the autocorrelation functions obtained with a single realization of a random-phase thermal wavefunction and an average over 17 realizations of random-phase thermal wavefunctions. An oscillatory behavior indicating coherent vibrational dynamics is evident. This coherent dynamics survives the angular momentum averaging as can be seen in Fig. 3(a) (blue line). These results are an indication that coherent dynamics is distilled from an initial thermal ensemble. The probing of this coherent vibrational dynamics into the Π_u states (see above) produces a corresponding oscillatory pump–probe trace that its Fourier spectrum is shown in Fig. 4(b) (purple line) together with the experimental results. It shows a prominent peak at a frequency of 7.2 THz. As described above, the theoretical calculations account here only for the vibrational dynamics on the $(1)^1\Pi_g$ state. As seen in Fig. 4(b), the calculated vibrational Fourier peak is located at the same region of the experimental values, however it is much narrower. We attribute the difference between the experimental and theoretical results to the large uncertainty with regard to the calculated Π_u states due to their corresponding strong non-adiabatic coupling (see above).

4 Prospects for coherent control

The experimental and theoretical evidence for coherent dynamics distilled out of the initial thermal state means that coherent control should be possible. The most

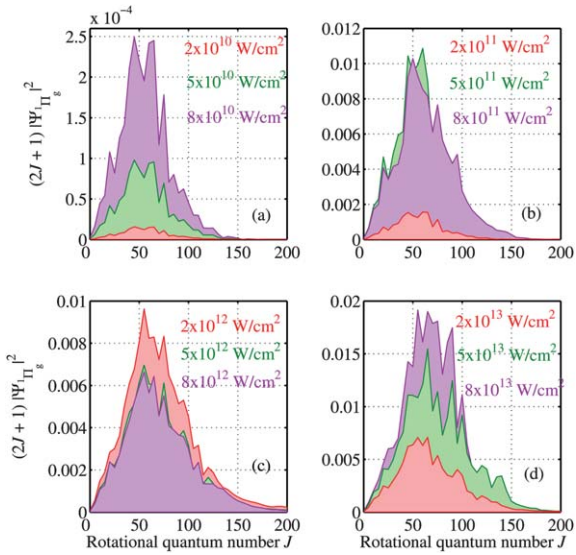

Fig. 2 Thermally averaged population transferred by the 70 fs 840 nm photoassociating pulse *via* two-photon transition to the $(1)^1\Pi_g$ excited state as a function of the initial rotational quantum number J (initial angular momentum) for different intensities. Notice that each panel has a different scale. The highest excitation probability calculated for the experimental intensity of 5×10^{12} W cm^{-2} is at $J = 55$. In general, the peak of the distribution moves to higher J as the intensity increases.

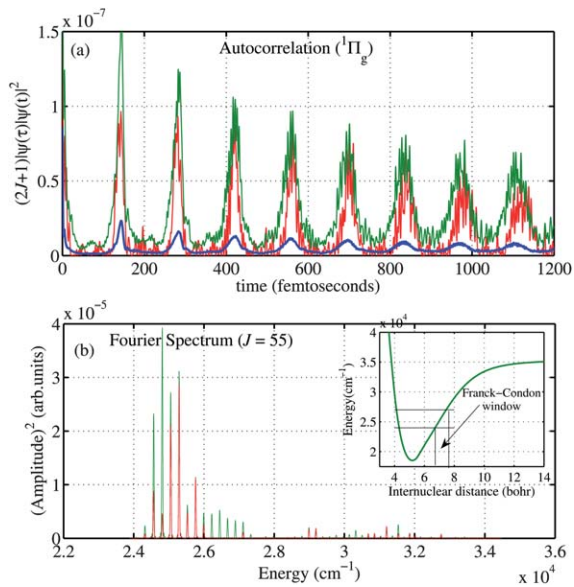

Fig. 3 Autocorrelation function of the transient molecular dynamics on the $(1)^1\Pi_g$ excited state potential for a fixed rotational quantum number $J = 55$ and $T = 1000$ K. (a) The autocorrelation as a function of time. The red curve represents a single realization of random phases, while the green curve has been obtained by averaging over 17 realizations. The blue curve results from an averaging over all the initial rotational quantum numbers (initial angular momentum). (b) The Fourier transform of the autocorrelation function. The inset shows the corresponding range of state energies that are populated on the $(1)^1\Pi_g$ state.

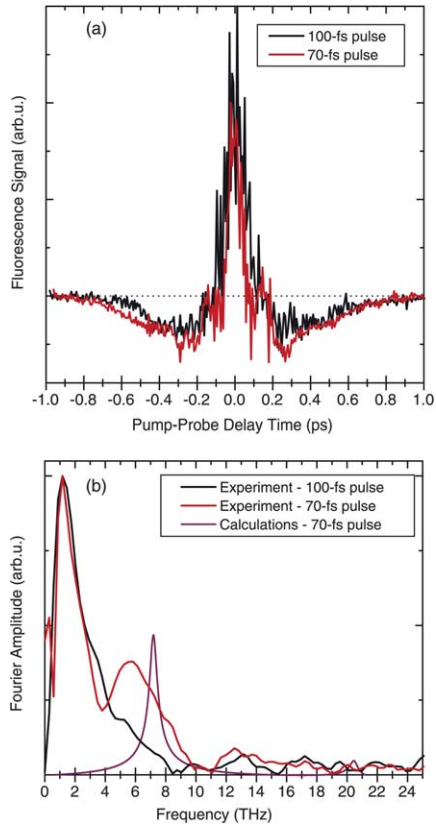

Fig. 4 Bandwidth dependence of the experimentally observed fluorescence signal after excitation with transform-limited femtosecond pulses: (a) the pump–probe signal trace and (b) Fourier spectrum of the trace. The two pulse durations are 70 fs and 100 fs. The probed vibrational coherence is attenuated for the excitation with the 100 fs pulse as compared to the excitation with the 70 fs pulse. The calculated Fourier spectrum for the case of 70 fs pulse is also shown. Note that the theoretical calculations account only for the vibrational dynamics on the excited state (see text).

obvious target is to enhance the production of photoassociated Mg_2 molecules. Other targets could be control of the emission signal.[27] Experimentally, such a target could also be optimized by random feedback techniques.[28] In the present context we demonstrate phase-only control as could be achieved by a pulse shaper. We also show intensity effects.

4.1 Chirp effects

The most simple phase control is a linear chirp, *i.e.*, a time-dependent frequency change. Experimentally it can be obtained by adding a dispersive element to the pulse generator. More elaborate phase control is obtained in the frequency domain by a pulse shaper. In strong fields positive chirp enhances population transfer.[29,30] This is because the dynamics on the excited state does not interfere with the population transfer. In a two-photon transition the chirp effect adds up. We simulate the effect by employing the following pulse form in the time domain *cf.* eqn (4):

$$S_c^2(t) = \frac{E_0^2 \sigma_t}{\sqrt{\sigma_t^4 + 16\chi_{II}^2}} e^{-\frac{t^2\sigma_t^2}{\sigma_t^4+16\chi_{II}^2}} \quad (13)$$

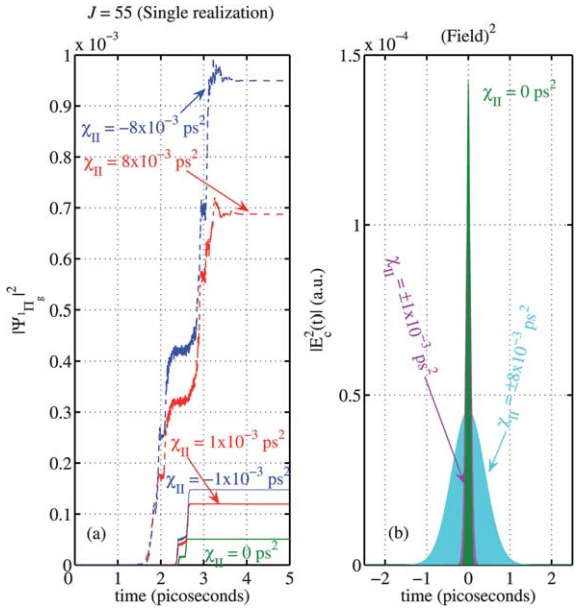

Fig. 5 The effect of the pulse chirp on the population in the $(1)^1\Pi_g$ excited state as calculated for the 70 fs transform-limited pulse and several cases of positive and negative chirps rates. The pulse fluence is kept constant in all the presented cases. The intensity of the (unchirped) transform-limited pulse is 5×10^{12} W cm^{-2}.

and the phase becomes *cf.* eqn (9):

$$\phi(t) = \frac{\chi_{II} 4t^2}{\sigma_t^4 + 16\chi_{II}^2} \tag{14}$$

where χ_{II} is the two-photon chirp rate in the frequency domain and σ_t is the transform limited pulse width. Eqn (13) reflects the fact that the chirped pulse is stretched in time with respect to the transform-limited pulse with peak intensity attenuated to keep the pulse fluence constant. The transform limited intensity is obtained by $I_0 = \frac{1}{2} c\varepsilon_0 E_0^2$, where c is the speed of light and ε_0 is the free space permittivity.

Fig. 5 shows the influence of a positively and negatively chirped pulse relative to the transform-limited pulse. In all cases the chirp enhances the population transfer with more than an order of magnitude enhancement for $\chi_{II} = \pm 8 \times 10^{-3}$ ps^2. For large chirp rates the positive and negative chirps lead to different enhancements, which is consistent with the theoretical predictions.[30] We expect the chirp enhancement to survive thermal averaging.

4.2 Intensity effects

The two-photon population transfer to the excited $(1)^1\Pi_g$ state is shown as a function of the initial angular momentum J for different intensities in Fig. 2. As the intensity increases, the peak of the distribution shifts to larger J values. For the intensity value used in the experiment, $\sim 10^{12}$ W cm^{-2}, the peak has its maximum at $J = 55$. This represents a compromise between a favorable Franck–Condon window and increasing phase space with J. Other minor peaks could be associated with rotational resonances.

5 Summary and conclusions

We have investigated femtosecond photoassociation of thermally hot atoms in the gas phase and its coherent control. In the photoassociation process, formation of

a chemical bond is facilitated by light in a free-to-bound optical transition. We have demonstrated photoassociation of hot atoms experimentally by measuring fluorescence resulting from the absorption of $(2 \oplus 1)$ photons. The Fourier transform of the experimental signal reveals molecular coherence of both vibrational and rotational nature in the intermediate electronically excited state that is accessed by the two-photon photoassociating transition. Our simulations also show molecular coherence of the photoassociated molecules. The theoretical model is based on a state-of-the-art treatment of the electronic structure of Mg_2 including *ab initio* two-photon couplings and dynamic Stark shifts and a novel quantum molecular dynamics approach to modeling a thermal ensemble subject to coherent excitation.

The significance of coherently controlling femtosecond photoassociation is twofold. On one hand, it addresses the fundamental problem of coherently controlling a system having an initial state that is an incoherent thermal mixture of different scattering states. In thermal equilibrium the scattering states correspond to eigenstates of the ground state Hamiltonian. On the other hand, success of femtosecond control of free-to-bound photoassociation is an example of coherent control of a photo-induced bimolecular chemical reaction. Chemical reaction control is a long-standing goal from the early days of the field of coherent control as a possible means for inducing new chemical reactions. Despite its importance, femtosecond control of the photoassociation of 'hot' thermal atoms has previously been investigated experimentally by only a single pioneering study more than a decade ago,[8,31–37] demonstrating only the basic feasibility of spectroscopy of hot atom-atom photoassociation with subsequent rotational coherence using unshaped femtosecond pulses.

Acknowledgements

Financial support from the Deutsche Forschungsgemeinschaft through the Emmy Noether programme and SFB 450 is gratefully acknowledged. This research was supported by The Israel Science Foundation (Grant No. 1450/10) and by The James Franck Program in Laser Matter Interaction. RM and MT would like to thank the Polish Ministry of Science and Higher Education for the financial support through the project N N204 215539. MT was supported by the project operated within the Foundation for Polish Science MPD Programme co-financed by the EU European Regional Development Fund.

References

1 D. J. Tannor and S. A. Rice, *J. Chem. Phys.*, 1985, **83**, 5013.
2 S. A. Rice, *Science*, 1992, **258**(5081), 412.
3 S. A. Rice and M. Zhao, *Optical control of molecular dynamics*, John Wiley & Sons, 2000.
4 P. Brumer and M. Shapiro, *Principles and Applications of the Quantum Control of Molecular Processes*, Wiley Interscience, 2003.
5 C. P. Koch, M. Ndong and R. Kosloff, *Faraday Discuss.*, 2009, **142**, 389.
6 T. Brixner and G. Gerber, *ChemPhysChem*, 2003, **4**(5), 418.
7 O. Kühn and L. Wöste, editors, *Analysis and control of ultrafast photoinduced reactions*, Springer, Berlin, 2007.
8 U. Marvet and M. Dantus, *Chem. Phys. Lett.*, 1995, **245**(4-5), 393.
9 W. Salzmann, T. Mullins, J. Eng, M. Albert, R. Wester, M. Weidemüller, A. Merli, S. M. Weber, F. Sauer, M. Plewicki, F. Weise, L. Wöste and A. Lindinger, *Phys. Rev. Lett.*, 2008, **100**, 233003.
10 V. Zeman, M. Shapiro and P. Brumer, *Phys. Rev. Lett.*, 2004, **92**, 133204.
11 C. P. Koch, R. Kosloff, E. Luc-Koenig, F. Masnou-Seeuws and A. Crubellier, *J. Phys. B: At., Mol. Opt. Phys.*, 2006, **39**, S1017.
12 C. P. Koch and R. Kosloff, *Phys. Rev. Lett.*, 2009, **103**, 260401.
13 C. P. Koch, R. Kosloff and F. Masnou-Seeuws, *Phys. Rev. A*, 2006, **73**, 043409.
14 W. Salzmann, U. Poschinger, R. Wester, M. Weidemüller, A. Merli, S. M. Weber, F. Sauer, M. Plewicki, F. Weise, A. Mirabal Esparza, L. Wöste and A. Lindinger, *Phys. Rev. A*, 2006, **73**, 023414.
15 B. L. Brown, A. J. Dicks and I. A. Walmsley, *Phys. Rev. Lett.*, 2006, **96**, 173002.

16 S. Amaran, R. Kosloff, M. Tomza, R. Moszyński, L. Rybak, Z. Amitay, and C. P. Koch, *in preparation*.
17 W. Skomorowski *et al.*, *in preparation*.
18 J. Olsen and P. Jørgensen, *J. Chem. Phys.*, 1985, **82**, 3235.
19 C. Hättig, O. Christiansen and P. Jørgensen, *J. Chem. Phys.*, 1998, **108**, 8331.
20 C. Hättig, O. Christiansen and P. Jørgensen, *J. Chem. Phys.*, 1998, **108**, 8355.
21 O. Christiansen, A. Halkier, H. Koch, P. Jørgensen and T. Helgaker, *J. Chem. Phys.*, 1998, **108**, 2801.
22 C. Hättig, O. Christiansen, S. Coriani and P. Jørgensen, *J. Chem. Phys.*, 1998, **109**, 9237.
23 C. Hättig, O. Christiansen and J. Gauss, *J. Chem. Phys.*, 1998, **109**, 4745.
24 R. Kosloff, *Annu. Rev. Phys. Chem.*, 1994, **45**, 145.
25 R. Kosloff, Time Dependent Methods in Molecular Dynamics, *J. Phys. Chem.*, 1988, **92**, 2087–2100.
26 U. Banin, R. Kosloff and S. Ruhman, *Chem. Phys.*, 1994, **183**, 289.
27 L. Rybak, L. Chuntonov, A. Gandman, N. Shakour and Z. Amitay, *Opt. Express*, 2008, **16**, 21738.
28 R. S. Judson and H. Rabitz, *Phys. Rev. Lett.*, 1992, **68**(10), 1500.
29 S. Ruhman and R. Kosloff, *J. Opt. Soc. Am. B*, 1990, **7**, 1748.
30 J. Vala and R. Kosloff, *Opt. Express*, 2001, **8**, 238.
31 P. Backhaus and B. Schmidt, *Chem. Phys. Lett.*, 1997, **217**, 131.
32 P. Gross and M. Dantus, *J. Chem. Phys.*, 1997, **106**, 8013.
33 U. Marvet, Q. Zhang and M. Dantus, *J. Phys. Chem. A*, 1998, **102**, 4111.
34 P. Backhaus, B. Schmidt and M. Dantus, *Chem. Phys. Lett.*, 1999, **306**(1-2), 18.
35 R. de Vivie-Riedle, K. Sundermann and M. Motzkus, *Faraday Discuss.*, 1999, **113**, 303.
36 P. Marquetand and V. Engel, *J. Chem. Phys.*, 2007, **127**, 084115.
37 E. F. de Lima, TS Ho and H. Rabitz, *Phys. Rev. A*, 2008, **78**, 063417.

